International Journal of Heat and Mass Transfer 52 (2009) 5309–5322

Contents lists available at ScienceDirect

International Journal of Heat and Mass Transfer

journal homepage: www.elsevier.com/locate/ijhmt

Influence of channel aspect ratio on heat transfer in rotating rectangular ducts with skewed ribs at high rotation numbers

T.-M. Liou [a,*], S.W. Chang [b], J.S. Chen [a], T.L. Yang [b], Yi-An Lan [b]

[a] *Department of Power Mechanical Engineering, National Tsing Hua University, 30013 Hsinchu, Taiwan, ROC*
[b] *Department of Marine Engineering, National Kaohsiung Marine University, 811 Kaohsiung, Taiwan, ROC*

ARTICLE INFO

Article history:
Received 8 January 2008
Accepted 6 July 2009
Available online 24 August 2009

Keywords:
Rotating ribbed duct
Channel aspect ratio
High rotating and buoyancy numbers
Hear transfer augmentation

ABSTRACT

Centerline heat transfer measurements along two opposite ribbed walls in three rotating rectangular ducts roughened by 45° staggered ribs with channel aspect ratios (AR) of 1:1, 2:1 and 4:1 are performed at Reynolds (*Re*), rotation (*Ro*) and buoyancy (*Bu*) numbers in the ranges of 5000–30,000, 0–2, and 0.005–8.879, respectively. These channel geometries are in common use as the internal cooling passages of a gas turbine rotor blade and the tested *Ro* and *Bu* ranges are considerably extended from the previous experiences. This study focuses on the heat transfer characteristics in response to the change of AR under the parameter ranges examined. With zero-rotation ($Ro = 0$), the local Nusselt numbers (Nu_0) along the centerlines of two opposite ribbed walls increase as AR increases due to the increased rib-height to channel-height ratio. The *Bu* impact on heat transfer appears to be AR dependent, i.e. the increase of *Bu* elevates Nusselt number ratios Nu/Nu_0 in the square channel but impairs heat transfer in the rectangular channels of AR = 2 and 4. Acting by the Coriolis effect alone, all the leading edge *Nu* values in the present *Ro* range are lower than the zero-rotation references but started to recover as *Ro* increases from 0.1 in the channels of AR = 1, 2 and from 0.3 in the channel of AR = 4. The trailing edge Nu/Nu_0 ratios increase consistently from unity as *Ro* increases but their responses toward the increase of AR are less systematic than those found along the leading edge. The above findings, with the aids of extended *Ro* and *Bu* ranges achieved by this study, serve as the original contributions for this technical community. The Nu/Nu_0 ratios in the rotating channels of AR = 1, 2, and 4 fall in the ranges of 0.6–2.2, 0.5–2.7, and 0.5–2.1, respectively. A set of heat transfer correlations is derived to represent all the heat transfer data in the periodically developed flow regions of three rotating ducts.

1. Introduction

A gas turbine rotor blade is running in the harsh environment with extremely high mechanical and thermal loads. Its life span heavily relies on the cooling technology applied to the rotor blade in which the airflow extracted from the compressor circulates through the internal cooling passages. Surface ribs, pin-fins and 180° turns connecting the serpentine passages are in general uses to formulate the cooling network inside a rotor blade. Following the blade profile from the blade-nose, midchord, to trailing edge, the cross-sections of these internal coolant passages vary from the trapezoidal, rectangular, to nearly triangular sections. The secondary flows induced by rotation and skewed ribs are found to generally promote the exchange of near-wall hot fluid and core-region cold fluid and, in turn, the heat transfer performance. However, the strength of the secondary flow is also affected by the cross-sectional shape of coolant passage. This fact draws much attention to examine the heat transfer in the rotating channels with various cross-sectional shapes [1–18]. Fig. 1 compares the experimental and numerical heat transfer results on two opposite stable (Fig. 1(a)) and unstable (Fig. 1(b)) ribbed walls of the rotating channels with square [4–6,14], rectangular [7,12–14], triangular [15], circular [16], and trapezoidal [17,18] cross-sections. The variations of Nusselt number ratio (Nu/Nu_0) with rotating number (*Ro*) for these rotating channels [4–7,12–18] are clustered into a similar trend that respectively characterizes the typical *Ro* effects on heat transfer over the stable or unstable wall. The data scatterings around each "shape" controlled data trend (see Fig. 1(a) or (b)) reflect various degrees of rotating buoyancy effects in these rotating ribbed channels of different cross-sectional shapes and rib configurations. Differentiations of these rotating buoyancy effects [4–7,12–18] are not assessable in Fig. 1 and remain unsolved. Nevertheless, the heat transfer rates on the unstable wall are consistently improved over those on the stable wall as *Ro* increases for all the heat transfer results summarized in Fig. 1. This agreement again confirms that the aforementioned Coriolis secondary flows perpendicular to the main flow direction tend to drive the

---

[*] Corresponding author. Tel.: +886 3 5742607.
E-mail address: tmliou@pme.nthu.edu.tw (T.-M. Liou).

0017-9310/$ - see front matter © 2009 Elsevier Ltd. All rights reserved.
doi:10.1016/j.ijheatmasstransfer.2009.07.013

Nomenclature

English symbols

AR	channel cross-sectional aspect ratio (=W/H)
A, n	coefficient
Bu	Buoyancy number ($= Ro^2\beta(T_w - T_b)(R/d)$)
C_p	specific heat of fluid (J kg^{-1} K^{-1})
d	hydraulic diameter of test duct (m)
e	rib height (m)
f_s	functional coefficients
H	channel height (m)
k	thermal conductivity of fluid (W m^{-1} K^{-1})
l	rib land (m)
Nu	rotational Nusselt number ($= qd/[k(T_w - T_b)]$)
Nu_0	zero rotation Nusselt number
Nu_∞	Nusselt number value for stationary developed turbulent duct flow
P	rib pitch (m)
Pr	Prandtl number ($= \mu C_p/k$)
q	convective heat flux (W m^{-2})
R	mid-span eccentricity of test channel (m)
Re	Reynolds number ($= \rho W_m d/\mu$)
Ro	Rotating number ($= \Omega d/W_m$)
T_b	fluid bulk temperature (K)
T_w	wall temperature of test duct (K)
W	channel width (m)
W_m	mean through flow velocity (m s^{-1})
x	axial location from flow entrance along the centerline of ribbed wall (m)
X	dimensionless axial location ($= x/d$)

Greek symbols

α	rib angle of attack (°)
β	thermal expansion coefficient of fluid (K^{-1})
ρ	fluid density (kg m^{-3})
μ	fluid dynamic viscosity (kg s^{-1} m^{-1})
Ω	rotating speed of test duct (rad s^{-1})
Ψ, ϕ_1, ϕ_2	unknown functions

Subscripts

L	refers to centerline of rotating leading wall
T	refers to centerline of rotating trailing wall
R	refers to rib-top location
MR	refers to mid-rib location between a rib pitch
0	refers to non-rotating situation

relatively cool fluids from the central core region towards the unstable side of a rotating channel with arbitrary cross-sectional shape. The different Nu/Nu_0 ratios found in the rotating ribbed ducts of various cross-sectional shapes [4–7,12–19] reflect the various modes of interactions between the secondary flows induced by the ribs and the Coriolis forces. It is noticed that, among the comparative groups collected in Fig. 1, the heat transfer performances in the rectangular ribbed channels are sensitive to the channel aspect ratio (AR) [12–14]; however, the majority of heat transfer data available to date is limited at the low Ro ranges ($Ro \leqslant 0.3$).

The early studies of AR impacts on heat transfer in rotating rectangular channels with smooth walls [8,9] incorporated the AR effects in the momentum equations as $Ro/(\mathrm{AR} + 1)$ so that the AR ratio was treated as a controlling parameter. As a result, the rotating Coriolis effects are weakened in the channels with high AR ratios and tend to be diminished as AR approaches infinite. The experimental results of $Ro \leqslant 0.28$ in [8] were in favor of their theoretical treatments and showed that the mean Nu/Nu_0 ratios followed the regular order of square, low AR, and high AR ducts. However, for higher values of Ro and AR, the pair of counter-rotating Coriolis secondary vortices separated into smaller multi-cells so that the regular order of heat transfer performances reported in [8] was not followed in [9]. In a recent numerical study [11], the combined effects of rotation and turn in a two-pass rectangular channel with smooth walls had led to the generation of asymmetric vortex pair (Coriolis secondary flows) with larger vortex and thus more pronounced heat transfer near the leading surface in the channels of AR = 1/2 and 1/4. The results agreed with the previous studies [8,9] at lower values of Ro ($\leqslant 0.28$).

In the rotating rectangular channels with surface ribs, the rib generated secondary flow together with the rotating induced Coriolis secondary flow further complicate the correlation between AR and heat transfer. Numerical heat transfer studies [12,13] and mass transfer measurements using the naphthalene sublimation method with $Ro \leqslant 0.4$ [14] had demonstrated the significant AR effects on the fluid flow and heat transfer through their impacts on the strength of the Coriolis secondary flow and the area fraction of the ribbed surface. The numerical results indicated a more intense Coriolis secondary flow in the channel with a smaller AR but a more intense rib-induced secondary flow in the channel with a larger AR [12,13]. Although the overall heat/mass transfer rate increased with increasing AR in the stationary channel due to the high rib height-to-duct height ratio, the heat transfer enhancements along the unstable ribbed walls of the rotating two pass channel systematically decreased as AR increased from 0.5, 1 to 2. The orthogonal mode rotation affected less dominantly as AR increased for the duct with transverse ribs [14]. Nevertheless, the absence of buoyancy when the mass/heat transfer data are acquired by the naphthalene sublimation method has obviated the exploration of rotating buoyancy (Bu) on heat transfer. The difficulties of performing experiments to capture the full field heat transfer information at the rotating conditions with buoyancy effects involved have also prevented the further progress of experimental studies in this field.

Although some previous studies [12–14] have investigated the effect of AR on turbulent heat transfer in rotating rectangular ribbed channels at low Ro ($Ro \leqslant 0.4$ in Fig. 1), the AR effects concluded for the low Ro cases [12–14] may not be applicable in the high Ro range. It is noted that the typical gas turbine engines operate at speeds of 3000–20,000 rpm with Reynolds number (Re) up to 100,000 resulting in a maximum Ro of 2 in the internal coolant passages of rotor blades. In Fig. 1 the few scattered data points in the range of $0.3 < Ro < 1$ urge the extension of data range to emulate more realistic engine conditions by extending Re, Ro, and Bu simultaneously. For the future developments of turbine rotor blades, the academia has made every endeavor to fill the unknown data points in the range of $0.4 < Ro < 2$. Thus, this study is aimed at examining the AR effects on turbulent heat transfer in the orthogonally rotating rectangular duct with skewed ribs for $0 \leqslant Ro \leqslant 2$ and $0.005 \leqslant Bu \leqslant 8.879$. Following our previous experimental approach [17–19], the present study generates a set of heat transfer data in the parametric range of $Re \times Ro \leqslant 10{,}000$ and $Ro \leqslant 2$ for three rotating rectangular ducts of AR = 1, 2, and 4 with a set of staggered 45° ribs of the same configuration. The experimental results reported in [18] for the similar rectangular rotating ribbed channel with AR = 2 are included and re-processed to compare with the heat transfer data generated from the present rotating ribbed channels with AR = 1 and 4. In general, the parametric studies of heat transfer in rotating passages adopt the flow parameters of

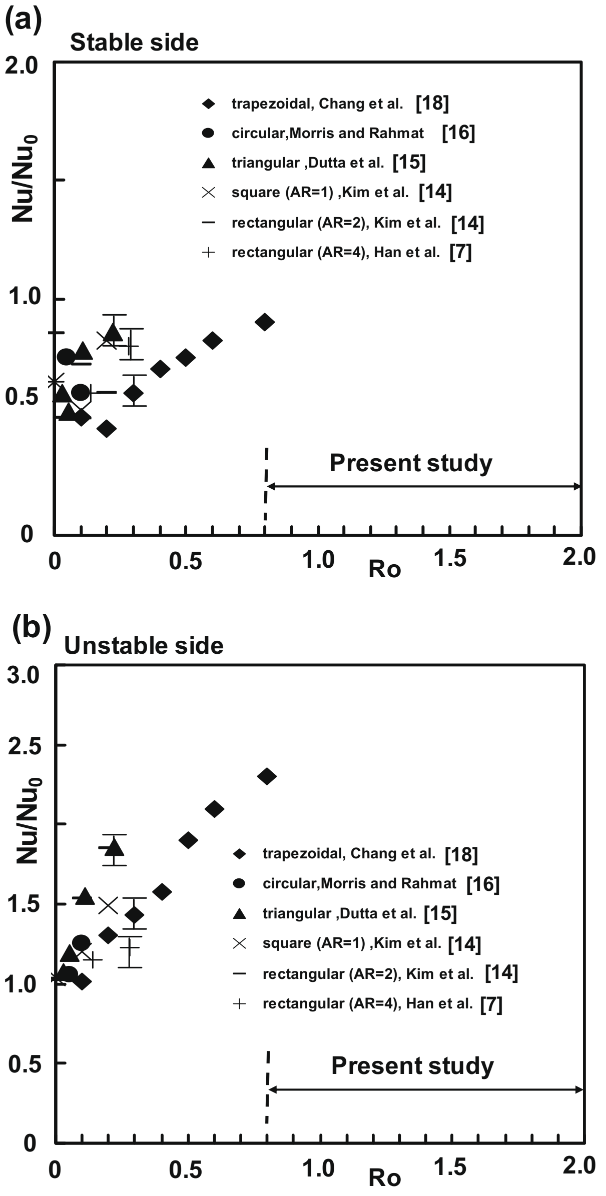

Fig. 1. Comparison of heat transfer performances in rotating ribbed channels with trapezoidal, circular, triangular, square, and rectangular cross-sectional shapes.

Re and *Ro* to characterize the relative strengths of forced convection and Coriolis forces in their own rights. The degree of rotating buoyancy effect is leveled by *Bu* in the form of $\Delta\rho/\rho\ Ro^2(R/d)$. This experimental study also determines and compares the individual and interactive influences of inertial and Coriolis forces with and without buoyancy interaction on heat transfer in three rotating rectangular ribbed ducts of AR = 1, 2, and 4. A set of heat transfer correlations of all the centerline heat transfer data is derived. It is worth noting that the skewed ribs and the Coriolis force cause significant heat transfer distribution in the transverse direction, which can not be detected by the limited thermocouple measurements. Nevertheless, at the representative rib and mid-rib locations the *local* heat transfer data generated by this study at the high *Ro* up to 2 have enabled a detailed parametric analysis and highlighted the interesting heat transfer physics in respect of individual and interdependent Coriolis and rotating buoyancy effects on local heat transfer. The major contribution of this work for this technical community is to parametrically examine the impacts of AR ratio on heat transfer in the rectangular duct roughened by 45° staggered ribs with *Ro* considerably extended to 2. The gathered heat transfer correlations are useful for CFD validation and serve as the design references for the internal coolant channels of gas turbine rotor blades.

2. Details of experiments

2.1. Heat transfer test module

The rotating test rig (Fig. 2) having been previously described was commissioned to perform high pressure tests leading to the generation of heat transfer data in the range of $0 \leqslant Re \times Ro \leqslant 10{,}000$ [17]. For the present study, this rotating rig carries the 246 mm long heat transfer test module with the mid-span eccentricity (R) of 373 mm (Fig. 2(a)) at speeds up to 850 rpm. The test airflow is pressurized by two sets of screw-type compressor with the pressures inside the test section up to 3.5 bars. Prior to entering the heat transfer test module, the airflow is dehumidified and cooled to the ambient temperature through a refrigeration unit. The dehumidified airflow is then channeled from the air tank through a set of pressure regulator and filter, a pressure transducer, a mass flow meter and a needle valve at which the mass flow rate of coolant into the test section is adjusted and measured. In order to maintain the variations of *Re* and *Ro* at the flow entrance of the test section within ±1% of the targeting values, the mass flow rate of test coolant is frequently adjusted to compensate the variations of fluid properties.

Fig. 2(a) further shows the constructional details of the heat transfer test module with airflow in the radially outward direction. Three test sections are square and rectangular in cross-section with the channel width (rib-roughened wall) to channel height ratios of 1, 2, and 4. Each heat transfer test module is formulated with the identical design as typified in Fig. 2(a). The test section is made up of leading (1) and trailing (2) heated walls, together with two Teflon side walls (3). Four constituent walls of the test section are held together by means of a series of axial bolts to form the square or rectangular channel with the hydraulic diameter (d) of 30 mm. The rib-roughened heating foil (4) or (5) is produced by forging a continuous 0.1 mm thick stainless-steel foil with the width of 30, 45 or 75 mm for the channel of AR = 1, 2 or 4, respectively. The effective heating lengths for three test channels of AR = 1, 2, and 4 are 240, 246, and 246 mm, respectively. Centerline heat transfer measurements and heat fluxes are provided over two opposite rib-roughened leading (4) and trailing (5) foils. The 45° ribs forged from the continuous thin foil are arranged in the staggered manner on two opposite walls. The leading (4) and trailing (5) ribbed foils are connected in series through which the electrical power is supplied for joule heat. The basically uniform heat flux thermal boundary conditions are simulated over two ribbed surfaces. For such heating configuration, heat fluxes also issue from the top and side walls of each skewed rib simulating the heating condition different from those using the heating foil underneath a rib-roughened plate [4–6,15]. The surface areas of all skewed ribs are taken into account for the heat flux evaluation. The area ratios of the ribbing surface to the projected flat surface of each ribbed foil (4) or (5) are 1.19, 1.22, and 1.21 for the channels of AR = 1, 2, and 4, respectively. Electrical DC currents through the stainless-steel heating foils (4)(5) are controlled and metered by the power supply unit. For each tested *Re* and *Ro* condition, the buoyancy levels are varied by adjusting the heating power. Two ribbed heating foils are clamped between the top Teflon flange (6) and two bottom copper plates (7). These heating foils are sandwiched between a set of 3 mm thick copper plates underneath the top flange (6) to complete the electrical circuit. A replaceable orifice thread is fitted at the center of top Teflon flange (6) to adjust the

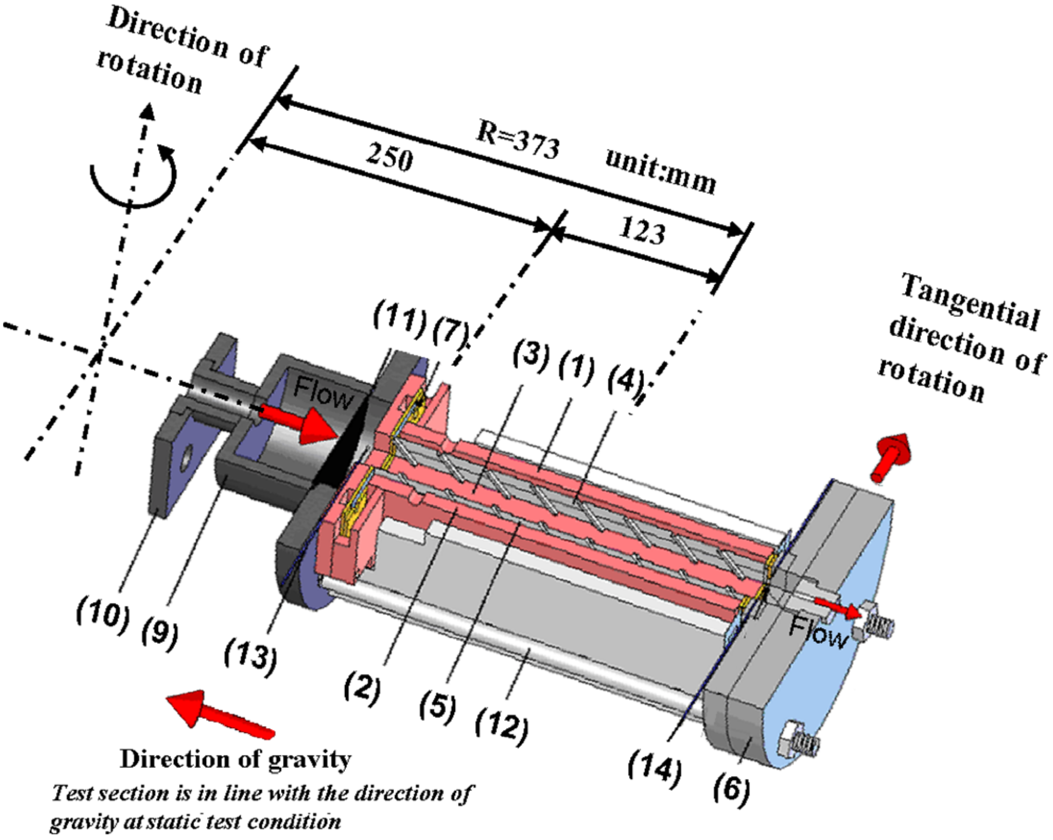

(1)	Leading wall	(7)	Copper plate
(2)	Trailing wall	(8)	Wall thermocouple (T_w)
(3)	Teflon side wall	(9)	Entry plenum chamber
(4)	Leading ribbed heating foil	(10)	End flange
(5)	Trailing ribbed heating foil	(11)	Mesh
(6)	Top Teflon flange	(12)	Draw bolt
(13)	Thermocouple measuring entry T_b	(14)	Thermocouple measuring exit T_b

Fig. 2. (a) Constructional details of heat transfer test module. (b) Rib and cross-section configurations of AR = 4 channel (dimension: mm).

pressure level in the test channel. The selection of test pressure and rotating speed allows both *Re* and *Ro* to be controlled at the predefined values.

Twelve K-type thermocouples (8) with equal intervals at the rib and mid-rib locations are sparkle-welded on the back of the stainless-steel heating foil to measure the centerline wall temperature distributions on the leading and trailing surfaces. The coordinate system and the locations of these thermocouples (8) are indicated in Fig. 2(b). At each thermocouple junction, the ceramic cement is applied to secure its position on the heating foil. Thermocouple wires and heater cables, which connect with the instrumentation and power slip rings, respectively, are taken out of the test section through the grooves machined on the Teflon leading and trailing walls. It is well known that the Coriolis force interacts with the rib-induced secondary flows to produce peripheral heat transfer variations over each rib-roughened surface. However, due to the limited channels of instrumentation slip-rings, the peripheral heat transfer variation over each rib-roughened surface is not investigated by present study. This research focuses on the parametric analysis of the isolated and interactive *Re*, *Ro*, and *Bu* effects on Nu/Nu_0 to reveal the thermal physics in respect of AR impacts on heat transfer in the rotating rectangular channels with skewed ribs.

The rib and channel configurations of three test channels share the same rib angle of attack, 45°, and are characterized by five dimensionless parameters of:

Channel width, W(30, 45, 75 mm)/channel height, H(30, 22.5, 18.75 mm) = 1, 2, 4.
Rib height, e(3 mm)/channel height, H(30, 22.5, 18.75 mm) = 0.1, 0.13, 0.16.
Rib height, e(3 mm)/channel hydraulic diameter, d(30 mm) = 0.1.
Rib pitch, P(30 mm)/rib height, e(3 mm) = 10.
Rib land, l(3 mm)/rib height, e(3 mm) = 1.

The entry cylindrical plenum chamber (9) (Fig. 2(a)) consolidates with the end flange (10) that is orthogonally mounted on the rotating platform. The abrupt flow entrance and the heating arrangement create simultaneous developments of thermal and hydraulic boundary layers from the immediate flow entry for each heat transfer test section. At the exit plane of the entry plenum chamber (9), several layers of fine mesh (11) are installed. The complete test assembly is tightened between the end and top flanges (6)(10) by four draw-bolts (12). Air leakages from any pair of jointed faces are prevented by means of ‘O’ ring seals.

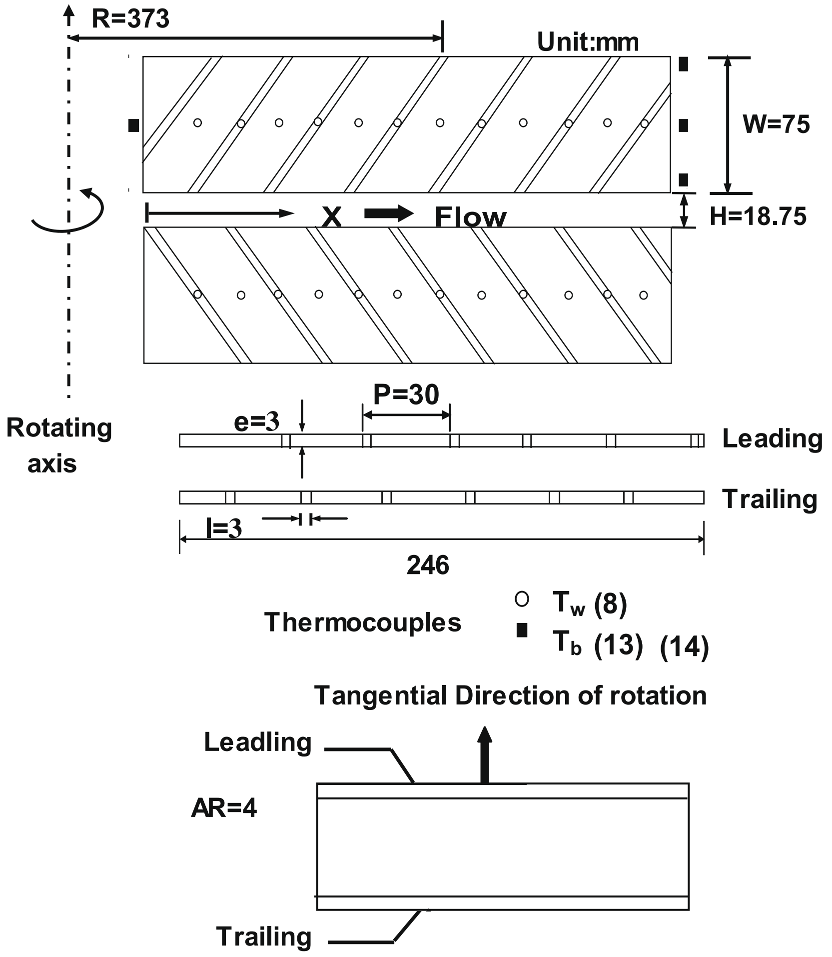

AR=(W/H)	1	2	4
H	30	22.5	18.75
W	30	45	75

Fig. 2 (*continued*)

The thermocouple (13) penetrating into the plenum chamber measures the entry air temperatures. The fluid properties used to evaluate *Re* and *Ro* at the flow entrance of the test section are calculated from the measured air inlet temperature during the period of data acquisition. The fluids properties used to define local *Re*, *Ro*, *Bu*, and *Nu* during the phase of the post data processing are based on the local fluid bulk temperatures. Three thermocouples (14) with equal interval at different spanwise locations on the exit plane of the test section as indicated in Fig. 2(b) detect the airflow exit temperatures. The fluid bulk temperature (T_b) at the exit plane of test section is evaluated as the average of three temperature measurements detected by three thermocouples (14). The enthalpy balance method is employed to calculate T_b at the axial locations where T_w are measured. The calculated T_b at the exit plane of the test section is constantly compared with the averaged measurements from thermocouples (14) to check the accuracy of energy accountancy. Experimental raw data are accepted only if the differences between the calculated and measured T_b values at the exit plane of the test section are less than ±10%. Thermal insulation fibers are wrapped around the outer surface of test module in order to minimize the external heat loss.

Table 1
Tested ranges of experimental non-dimensional groups

Non-dimensional parameter	Tested ranges (values)
Reynolds number (*Re*)	5000, 7500, 10,000, 12,500, 15,000
Rotation number (*Ro*)	0, 0.1, 0.3, 0.5, 0.7, 1, 1.3, 1.5, 1.7, 2
Buoyancy number [$Bu = \beta(T_w - T_b)Ro^2(R/d)$]	0.005–8.879, 0.093–8.789, 0.075–8.652
Density ratio [$\Delta\rho/\rho = \beta(T_w - T_b)$]	0.070–0.280, 0.076–0.294, 0.072–0.310

2.2. Dimensionless parameters in experimental study

The dimensionless momentum conservation equations expressed relative to a rotating reference frame as well as the energy equation reveal the following functional relationship of the non-dimensional groups that characterize the local heat transfer for a set of predefined geometrical and thermal boundary conditions [6].

$$Nu = \Psi\{Re, Ro, Bu, Pr, X\} \tag{1}$$

Definitions of all the dimensionless groups as well as their constituent symbols in Eq. (1) are defined in the Nomenclature section. The unknown Ψ function involves the inter-correlative relationships between *Re*, *Ro*, and *Bu* with *Nu*. A strategic aim of present study is to disclose the functional relationship of Eq. (1). With T_b varying from 31.7 to 89.2 °C, variations in Pr of coolant are limited within ±3.9% that is negligible. As a result, the Pr impact on heat transfer is disregarded from Eq. (1) for present study. The experimentally defined Nusselt number is evaluated as $Nu = qd/k(T_w - T_b)$. The local convective heat flux to the fluid is calculated by subtracting the external heat loss flux from the total heat flux supplied. The extent and characteristics of external heat loss flux are determined by means of a series of static and rotating heat loss calibrations tests that are individually performed prior to the heat convection tests. For this class of experimentation, the maximum heat loss is about 11.2% of the total heat flux supplied so that the basically uniform heat flux heating condition is acquired.

This parametric study of heat transfer performances in three rotating ribbed ducts with particular emphasis on the AR effects initiates from the examination of individual impacts of each governing flow parameter on heat transfer. The variation of each governing dimensionless group in Eq. (1), such as Re, Ro or Bu, for the set of pre-defined geometrical and thermal boundary conditions causes the corresponding Nu variations in respond to the isolated influence of the varied flow parameter. Comparisons of such isolated Ro and Bu impacts on heat transfer in three channels of AR = 1, 2, and 4 reveal the impacts of channel aspect ratio on heat transfer in the rotating rectangular ducts with skewed ribs. Table 1 summarizes the ranges of non-dimensional groups tested. It is noted that the maximum Re and Ro in Table 1 are not simultaneously attainable and the test range of $0 \leqslant Ro \leqslant 2$, which accordingly increases the Bu range, considerably extend the data range available in the open literature.

2.3. Experimental procedures

This experimental study has three phases for each heat transfer test section. Phase 1 generates the heat transfer results (Nu_0) at zero rotational speed to establish the reference data base against which the rotational heat transfer results (Nu) generated in phase 2 are compared to assess the general rotational effects on heat transfer. In phase 2 for each set of Re and Ro combination examined, heat transfer tests with five ascending heater powers to raise the highest wall temperatures to 75, 100, 125, 140, and 150 °C are performed that reveals the isolated rotating buoyancy effect on heat transfer. All the raw measurements are taken when the steady-state assumption is satisfied. A steady state condition is approximated when T_w variations for several successive scans are less than ±0.3 °C. In this respect, the time interval between two successive scans is about 1 min. Having satisfied the steady-state condition, all the relevant measurements such as heating powers, pressure levels, airflow rates and temperature measurements are stored and subsequently processed into the dimensionless groups defined in Eq. (1) with the fluid properties calculated from the local fluid bulk temperatures. The individual and interactive impacts of Re, Ro, and Bu on heat transfer are analyzed in phase 3 with a set of heat transfer correlations generated to calculate the local Nusselt numbers on rib and mid-rib locations in the periodically developed flow region for each test section. As the evaluation of experimental Nusselt number requires a finite wall-to-fluid temperature difference, the interactive Ro and Bu impact persists in the Nu data generated. In phase 3, an additional set of Nu data affected by Re and/or Ro impacts without buoyancy interaction is generated by extrapolating the rotational heat transfer data into the limiting condition of $Bu = 0$ with Re and Ro remain at finite values. The inclusion of the extrapolating heat transfer data at the so-called zero-buoyancy condition completes the entire set of heat transfer data.

The experimental uncertainties of the dimensionless groups in Eq. (1) are mainly attributed to the temperature measurements as the fluid properties are based on T_b. The test results with the higher heating power and the larger Reynolds number show the less experimental uncertainties. Following the method of estimating experimental uncertainties documented in ASME J. Heat Transfer [20], the maximum uncertainties for Nu, Re, Ro, and Bu are about 9.8%, 6.8%, 4.5%, and 7.4%, respectively, with the wall-to-fluid temperature differences in the range of 26–95 °C.

3. Results and discussion

3.1. Heat transfer results with zero rotation

To allocate the first rib on the corner of trailing wall (Fig. 2(b)), the centerline X-wise coordinates for the first rib locations are different in the channels of AR = 1, 2, and 4. Therefore, the comparisons of centerline streamwise heat transfer variations between the three tested channels are expressed at the rib and mid-rib (MR) locations as depicted in Fig. 3. The axial coordinates corresponding to each rib and mid-rib locations in the three channels are summarized in the table of Fig. 3. In these three ribbed channels with zero rotation, the centerline T_w measurements along the two opposite ribbed walls do not exhibit significant differences. But, due to the staggered arrangement of the skewed ribs, T_w differences between each pair of opposite measurements are caused by different rib and mid-rib locations. For present study with the direct thermocouple (TC) measurements on each heating foil, the T_w measurements are local values and the wall conduction effects that smooth out the wall temperature variations inside the plate-type ribbed wall are minimized. This type of T_w measurements leads to the generation of the valuable rib-top heat transfer data which can not be accurately acquired using the transient liquid crystal thermometry method or by the TC measurements from the plate-type ribbed wall. In each test channel, the axial T_w measurements exhibit the zigzag pattern with the lower wall temperatures at the rib-tops relative to their adjacent downstream mid-rib locations. As the experimental heating condition over each ribbed wall corresponds closely to the uniform heat flux, the fluid bulk temperatures increase linearly in the axial direction. The resultant axial Nu_0 variation reassembles the zigzag pattern of wall temperature profile with the higher Nu_0 levels at the rib-tops. By way of normalizing Nu_0 with Dittus–Boelter Nusselt number (Nu_∞) [21], heat transfer augmentations in these static ribbed channels from the references in smooth tube are revealed in terms of Nu_0/Nu_∞ for $Ro = 0$ and $Re = 10,000$. The relatively high Nu_0/Nu_∞ ratios in the initial entry region of each test channel approach the periodically zigzag pattern at Rib 5 and MR 5–6 locations. The so-called periodically developed Nu_0/Nu_∞ variations tend to develop after the fifth rib. The parametric analysis of heat transfer results in the static and rotating channels to be described later, including the derivations of Nu_0 and Nu correlations, is based on the heat transfer data collected from the periodically developed flow region.

The extent of data scatters designated by the data bars at each rib or mid-rib location in Fig. 3, due to the variation of $\Delta\rho/\rho$ from 0.12 to 0.27, is less than 5%, suggesting the negligible buoyancy impact on heat transfer in the three static channels. The Nu_0/Nu_∞ ratios shown in Fig. 3 respectively fall in the ranges of 2.22–2.46, 2.32–2.60, and 2.47–2.68 for the static ribbed channels of AR = 1, 2, and 4. In this respect, our previous study has demonstrated that such heat transfer increments due to the reduction of channel height but keeping the same rib-height to channel hydraulic-diameter ratio (e/d) is attributed to the increased rib-height to channel-height ratio from 0.1, 0.13, to 0.16 rather than the increase of AR from 1, 2, to 4 [23]. Also shown in Fig. 3 is the comparable data of Johnson et al. [4] and Fu et al. [22] that share the similar geometries of test channel (AR = 1) and rib-roughened surfaces.

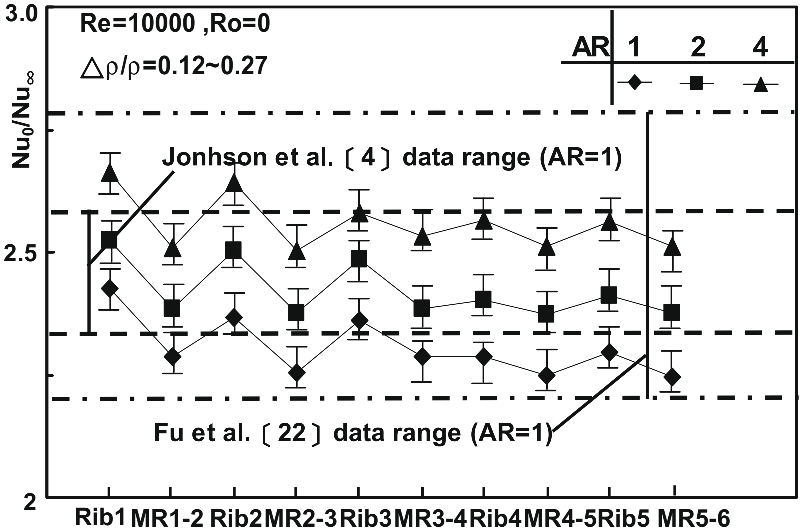

Axial locations (x/d) corresponding to the rib and mid-rib locations in the channels examined

AR	Rib 1	MR 1-2	Rib 2	MR 2-3	Rib 3	MR 3-4	Rib 4
1	0.512	1.110	1.521	2.012	2.500	3.010	3.501
2	0.716	1.182	1.649	2.116	2.520	3.018	3.453
4	1.510	2.010	2.567	3.110	3.567	4.200	4.667

Fig. 3. Comparison of axial variations of Nu_0/Nu_∞ in three static test channels of AR = 1, 2, and 4 at Re = 10,000.

Although the data ranges reported in [4] and [22] for the square ribbed duct are relatively large, the present heat transfer data in the test channel of AR = 1 fall in the range of Fu et al. [22] and are close to the range of Johnson et al. [4]. Agreements between the present heat transfer data and those reported in the open literature are satisfactory. Over the Re range of 5000–15,000, the review of the entire experimental heat transfer data shows that the Nu_0/Nu_∞ ratios are respectively in the ranges of 2.2–2.9, 1.6–4.3, and 2.4–4.7 for AR = 1, 2, and 4. In each ribbed channel, the ratio of Nu_0/Nu_∞ at each measurement spot decreases consistently as Re increases. The correlation of Nu_0 for each ribbed channel is no longer followed by the $Re^{0.8}$ relationship in the Dittus–Boelter formulation but followed by the Re exponent less than 0.8.

The dependence of Nu_0 on Re for the periodically developed flow region is individually examined for three ribbed channels. In Fig. 4, the variations of Nu_0 against Re in the periodically developed flow region for three test channels are compared. At rib 5 (Fig. 4(a)) and mid-rib 5–6 (Fig. 4(b)) locations, the increase of Nu_0 due to the increase of AR or Re is clearly revealed. As the variation of Pr is negligible for the present set of heat transfer data generated, each AR controlled data trend shown in Fig. 4(a) and (b) is correlated with the equation of $Nu_0 = A \times Re^n$ that automatically satisfies the limiting condition of $Nu_0 \to 0$ as $Re \to 0$ for the vanished forced convective capability at zero coolant flow. The A coefficient and n exponent derived for the periodically developed flow region in the rectangular channels of AR = 1, 2, and 4 with skewed ribs are both functions of AR as summarized in Table 2.

It is seen that the A coefficient decreases but the n exponent increases gradually with increasing AR. Substituting the functions A(AR) and n(AR) of Table 2 into $\boldsymbol{Nu_0 = A \times Re^n}$, one gets Eqs. (2) and (3) to evaluate the centerline Nu_0 level in the periodically developed flow region for a static rectangular channel of $1 \leqslant \text{AR} \leqslant 4$ with skewed ribs.

$$Nu_0 = -0.0772(\text{AR}) + 0.6295 \times Re^{0.025(AR)+0.5237} \quad \text{at rib location} \tag{2}$$

$$Nu_0 = -0.0859(\text{AR}) + 0.6045 \times Re^{0.0309(AR)+0.5218} \quad \text{at mid-rib location} \tag{3}$$

Eqs. (2) and (3) are treated as the benchmark references for assessing the effect of rotation on heat transfer in the three ribbed channels examined.

3.2. Generalized AR impacts on heat transfer in rotating test channels

Different Coriolis secondary flow structure can develop after the sharp turn of a rotating two-pass rectangular channel when its AR is varied [11]. The strength of the Coriolis secondary flow is affected by the value of AR as well [10–13]. In a rotating channel with angled ribs, the vortices induced by ribs are directed in the ribwise direction. Once the strength or/and the structure of the Coriolis secondary flows have been modified by AR, the result of local vortical cancellations or enhancements between the secondary flows induced by the Coriolis force and angled ribs is altered and, in turn, the resulted turbulent heat transfer performance is changed. For this reason the generalized rotational influences featured by the Re–Ro–Bu complex are discussed and compared using three sets of heat transfer data collected from the rotating channels of AR = 1, 2, and 4. The impacts of channel aspect ratio on rotational heat transfer can be thus revealed.

The Coriolis force causes the T_w measurements over the leading wall to be consistently higher than their trailing-edge counterparts. The spatial variations of fluid temperatures in a rotating channel trigger an intricate buoyancy interaction and lead to the combined Ro and Bu effects on heat transfer. The comparison of generalized rotational effects on heat transfer in three tested channels is typified by Fig. 5 that shows the axial variations of the normalized rotational Nussle number (Nu/Nu_0) at Re = 10,000 with Ro = 0.1, 0.3, 0.5, and 1. For each Re–Ro combination, the trailing edge (Fig. 5)(a)–(d) constantly operates with higher Nu/Nu_0 than its opposite leading edge (Fig. 5(e)–(h)). For each value of AR, the data band has respect to the increase of buoyancy level ($\Delta\rho/\rho$),

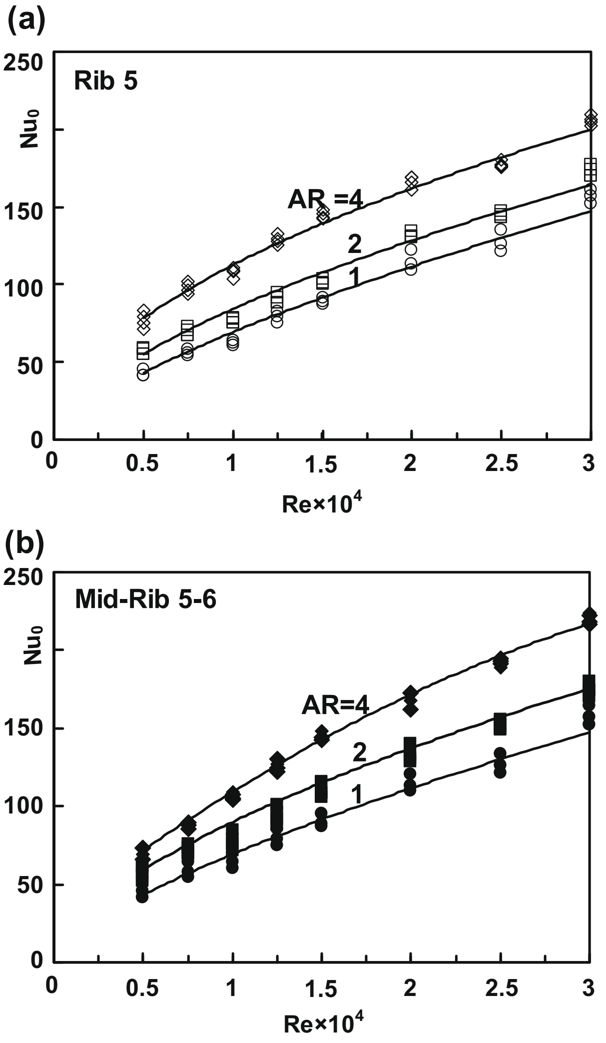

Fig. 4. Nu_0 versus *Re* in the periodically developed flow regions of three static test channels of AR = 1, 2, and 4 at (a) rib 5 and (b) mid-rib 5–6 locations.

as indicated by the hollow arrows. It is seen that the Nu/Nu_0 ratios increase with increasing $\Delta\rho/\rho$ in the square channel (AR = 1) but systematically decrease in the channels of AR = 2 and 4 as $\Delta\rho/\rho$ increases. The *Bu* ($=\Delta\rho/\rho\, Ro^2(R/d)$) impacts are reversed from improving heat transfer in the square ribbed channel to impeding heat transfer in the rectangular ribbed channels of AR = 2 and 4. In this respect, the work of Iskakov and Trushin [24] was the first to demonstrate that the rotating buoyancy effect could either enhance or impair heat transfer. But such different *Bu* impacts on heat transfer were caused by the operating thermal-fluid parameters rather than the geometric features of the rotating channel. Two early rotational heat transfer experiments undertaken by Morris group [25,2] reconfirmed the results of Iskakov and Trushin [24] in the respect of *Bu* impacts. Morris et al. [25,2] noticed that the presence of surface ribs had considerably suppressed the impacts of rotating buoyancy on heat transfer from the smooth-walled conditions. Although the dependency of *Bu* impacts on the geometric conditions of the rotating channel has been noticed [2], the reversed *Bu* effects on heat transfer in the rotating rectangular channels with angled ribs due to different values of AR have not been previously reported and will be further discussed in the later section of parametric study.

Table 2
Variations of *A* and *n* in $Nu_0 = A \times Re^n$ with AR.

AR	*A*		*n*	
	Rib	Mid-rib	Rib	Mid-rib
1	0.6023	0.5631	0.5423	0.5436
2	0.4010	0.3060	0.5863	0.5973
4	0.3456	0.2831	0.6236	0.6410

Comparing the three separate data series in each plot of Fig. 5, one can also observe the increase of AR for a given *Ro* consistently reduces the Nu/Nu_0 ratios along leading and trailing centerlines for the present *Ro* range. This observation clearly demonstrates the dependency of Coriolis effect on AR. It is worth noting that Nu_0 also varies with AR. When Nu/Nu_0 is cross-examined between the three test channels with different values of AR, one finds that Nu/Nu_0 denotes the degree of heat transfer modification from the static condition for each channel. As reported by several investigators [10–13], the strength of the Coriolis secondary flow is generally weakened as AR increases. However, when AR systematically increases, the side wall effects are also gradually confined to the region close to it. As a result, the typical one-pair structure of the Coriolis secondary flow in a square or circular rotating channel is accordingly yielded when AR increases. The local stabilizing and destabilizing effects on turbulent structures along the leading and trailing walls of the rotating channel are deemed to be affected by the value of AR. The experimental evidence reported in Fig. 5 suggests that the resultant flow structures in the rotating ribbed channels with larger AR will cause more pronounced heat transfer impediments along the leading centerline with less degree of heat transfer augmentation along the trailing centerline. The detailed flow measurements are required to clarify the flow physics for this heat transfer phenomenon.

The flow modifications resulting from the increase of AR have led to the modified *Ro*–*Bu* impacts on heat transfer and, in turn, further reductions of heat transfer levels in the rotating rectangular channels with skewed ribs. While the differences in Nu/Nu_0 ratios between the three test channels are less sensitive to the variation of *Ro* along the trailing edge, the three descending data series of different AR along the leading edge tend to be convergent as *Ro* increases. This leading-edge data trend has respect to the different critical values of *Ro* for three test channels. Above these critical *Ro* the leading-edge heat transfer starts to recover. As *Ro* increases, several previous studies [2,4,17,18] concluded that the leading edge heat transfer was initially reduced from the zero-rotation reference up to a critical *Ro* beyond which it started to recover and could even be elevated to a level above the zero-rotation reference at very high rotation number ($Ro \geqslant 1$). As a reconfirmation, for AR = 1 and 2 the present leading edge heat transfer starts to recover as $Ro > 0.1$ but for AR = 4 it needs $Ro > 0.3$ to recover, as will be shown shortly. Therefore, in the range of $0.1 < Ro < 0.3$, the leading-edge heat transfer levels are recovering in the channels of AR = 1 and 2 but still reducing in the channel of AR = 4. As a result, the heat transfer differences between the three test channels shown in Fig. 5(e) and (f) are relatively larger than those depicted in Fig. 5(g) and (h). The above discussed heat transfer variations in respond to *Ro*, *Bu*, and AR along both leading and trailing edges as demonstrated in Fig. 5 are similarly detected for all *Re* tested with five different heat flux settings and are treated as the generalized AR effects on heat transfer in rotating rectangular ducts with angled ribs.

3.3. Parametric analysis of heat transfer results in rotating channels

The parametric analysis using the heat transfer data generated from the three rotating ribbed ducts of AR = 1, 2, and 4 requires to reveal the individual and interactive impacts of *Re*, *Ro*, and *Bu*

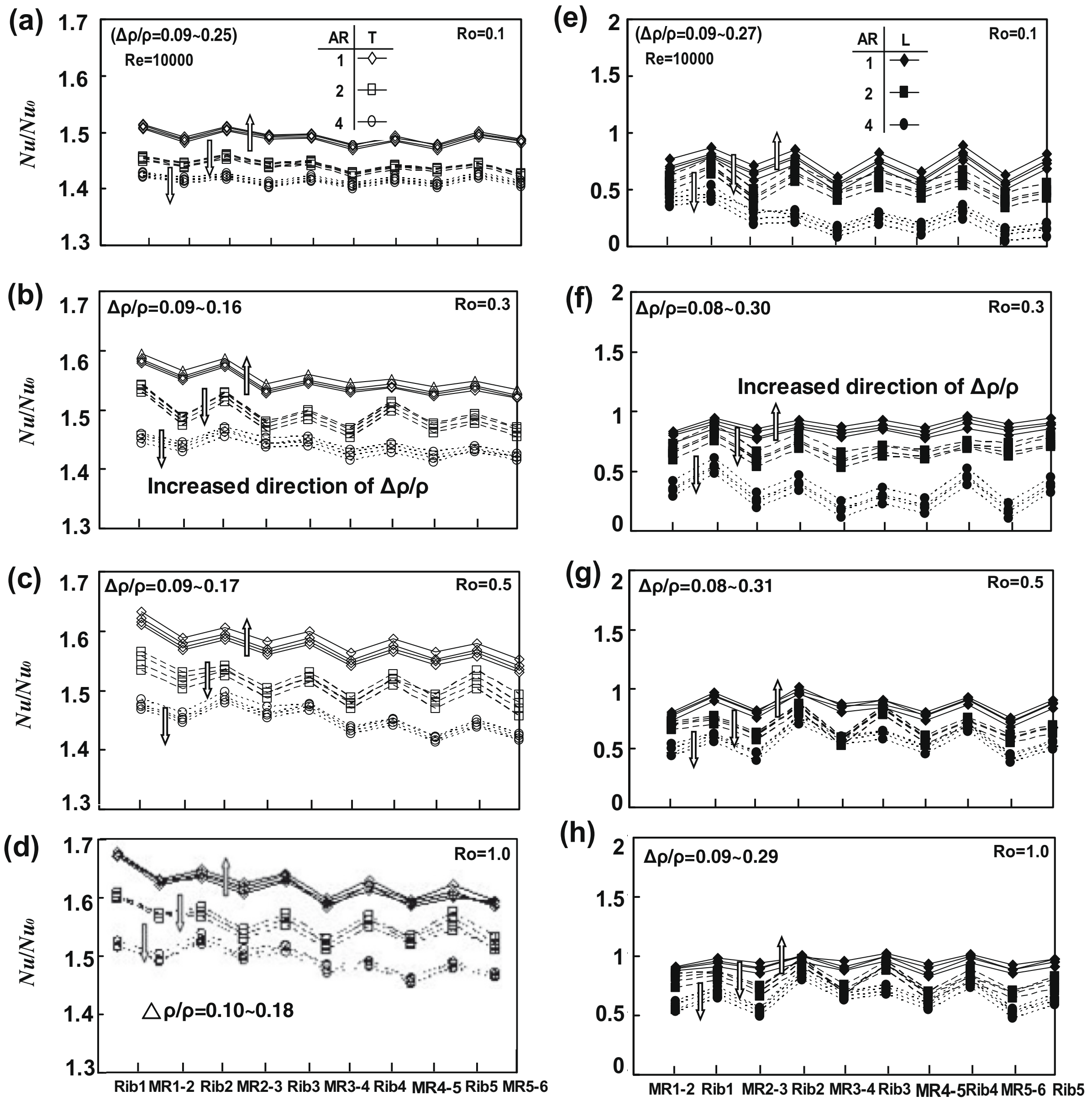

Fig. 5. Centerline variations of normalized rotational Nusselt number (Nu/Nu_0) in three rotating test channels of AR = 1, 2, and 4 at Re = 10,000 with Ro = 0.1, 0.3, 0.5, and 1.

on heat transfer. It is initially assumed that the Re effect can be uncoupled from the Ro–Bu complex and follow the Re^n relationship in the Nu_0 correlation where the n exponent is function of axial location and AR ratio. The assumption needs the normalized Nu/Nu_0 ratios to be functions of Ro and Bu but independent of Re. It is testified by checking the convergence of all the Nu/Nu_0 data obtained with 4–8 different sets of Re at a fixed Ro. Figs. 6 and 7, respectively, show the axial variations of Nu/Nu_0 ratio along trailing and leading edges in the three rotating test channels with Re in the range of 5000–30,000 at Ro = 0.1, 0.3, and 0.5 or 0.7. The data points collected in Figs. 6 and 7 are selected with similar ranges of $\Delta\rho/\rho$ in each test channel at a Ro examined so that the relative strength of the rotating buoyancy force for each set of comparable data remains at the similar level. It is observed that the three AR controlled data trends, converging from various Nu/Nu_0 results obtained with different Re at a fixed Ro in each test channel, indicate that the isolated Re effects from the Ro–Bu complex is applicable and featured by Re^n relationship. That is, data presentations in terms of Nu/Nu_0 ratios isolate the Re effects and are treated as the heat transfer results subject to the combined Ro–Bu impact. It is noticed that, although the density ratio ($\Delta\rho/\rho$) at each Ro examined is selected with a similar range, certain degrees of buoyancy interaction that respectively improve and impair heat transfer in the channels of AR = 1 and AR = 2 and 4 are affecting the Nu/Nu_0 data collected in Figs. 6 and 7. That the increase of AR from 1 to 4 systematically decreases the Nu/Nu_0 ratios is attributed to the combined Ro–Bu impacts. The highest heat transfer levels in the rotating square channel (AR = 1) as compared in Figs. 6 and 7 are resulting from the improving Bu effects on heat transfer opposite to the impairing Bu effects in the test channels of AR = 1 and 2. In the narrow channel of AR = 4, the Nu/Nu_0 ratios along the trailing and leading edges scatter in the ranges of 1.00–1.50 and 0.39–0.47 as shown in Figs. 6 and 7, respectively. Justified by the marked heat transfer reductions along the leading edge of the narrow channel with AR = 4, the influences of rotation are therefore considerable rather than less effective reported previously for the rotating ribbed channel of AR = 4 [14]. Relative to the conditions found in the test channels of AR = 1 and 2, the vortical interactions

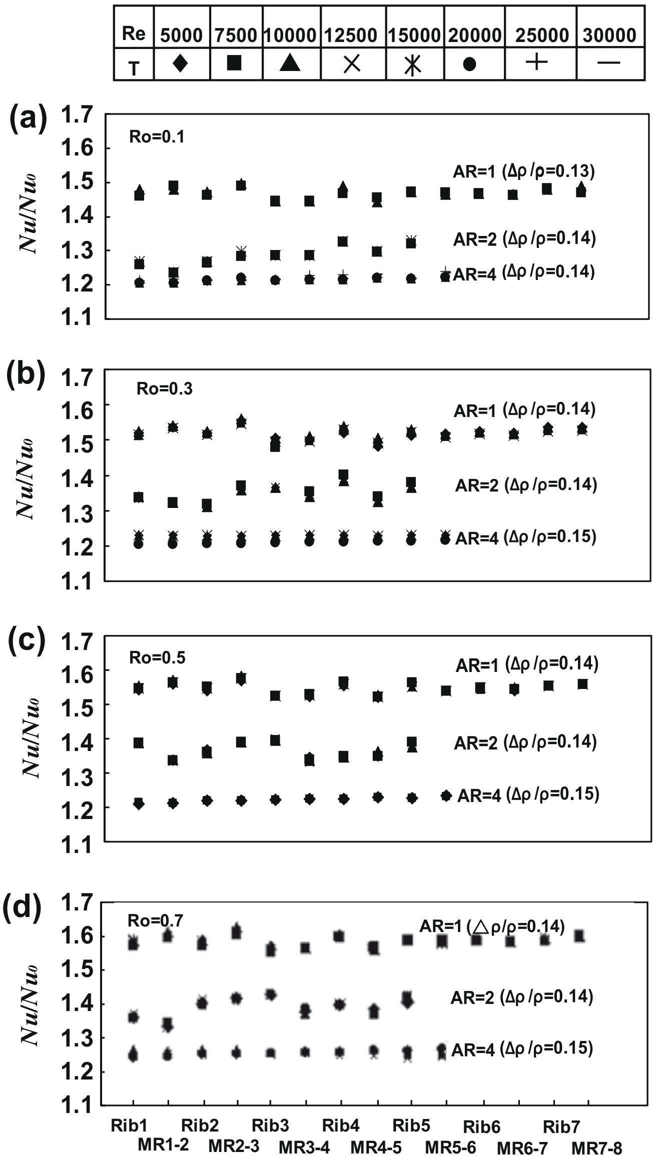

Fig. 6. Axial variations of Nu/Nu_0 ratio along trailing edge in three rotating test channels of AR = 1, 2, and 4 at Re = 5000–30,000 with fixed Ro of 0.1, 0.3, and 0.5 or 0.7.

between rib-flows and Coriolis-flows, as well as the rotation modified flow instabilities in the narrow channel (AR = 4), can considerably reduce the heat transfer levels along leading-edge centerline. In the rotating ribbed narrow channel of AR = 4, the vortical cancellation is severe or/and the turbulent activities are considerably suppressed, resulting in the lowest heat transfer ratios among three values of AR examined.

The subsequent procedure in the respect of parametric analysis is attempted to isolate Ro and Bu effects in the three rotating test channels. The determination of the so-called zero-buoyancy heat transfer data for the rotating test channels is essential in order to analyze the isolated Ro effects on heat transfer. As described previously, the extrapolation of Nu/Nu_0 data at each selected Ro into the limiting condition of $Bu = 0$ gives the heat transfer level corresponding to the zero-buoyancy condition at the selected Ro. Such procedure is illustrated in Fig. 8 that plots the variations of Nu/Nu_0 data against Bu for the three test channels at several fixed Ro. Data presentation in this manner can also examine the influences of Bu on heat transfer. Additionally, the data reported by

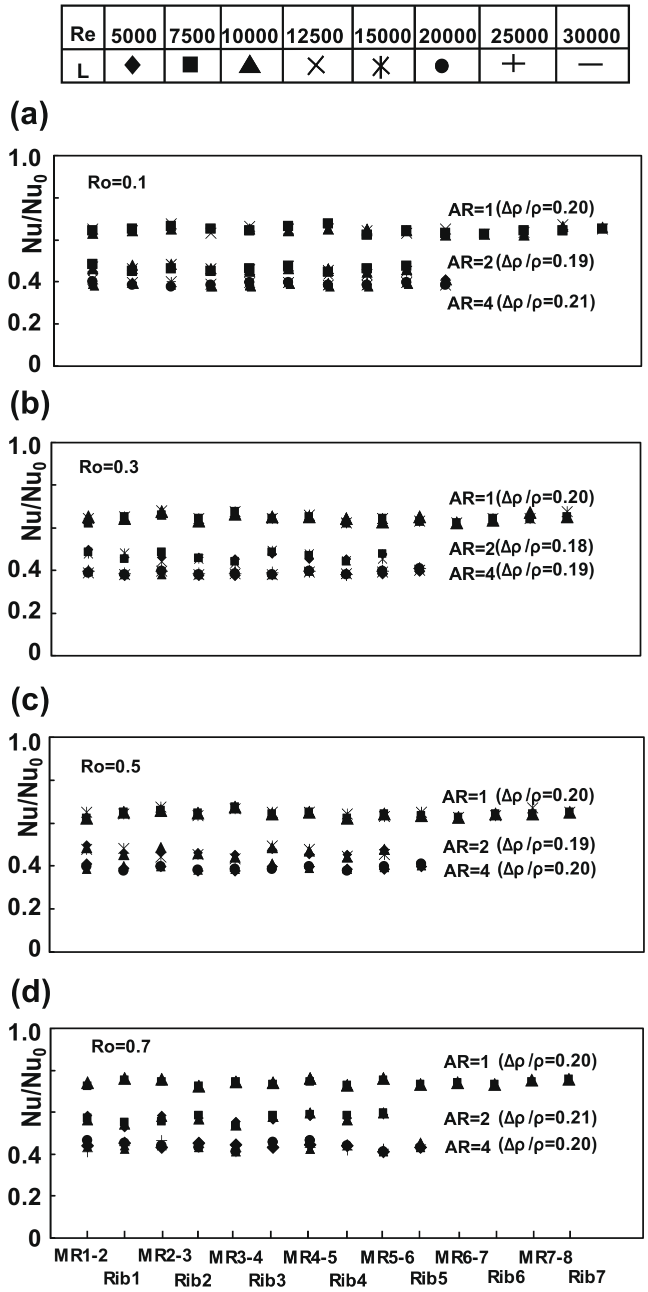

Fig. 7. Axial variations of Nu/Nu_0 ratio along leading edge in three rotating test channels of AR = 1, 2, and 4 at Re = 5000–30,000 with fixed Ro of 0.1, 0.3, and 0.5 or 0.7 (data points are produced in similar $\Delta\rho/\rho$ range for each test channel).

Johnson et al [4] for the square duct (AR = 1) with skewed ribs are included in Fig. 8(b) and (e) for comparison. Favorable agreements between the results of two research groups are attained. Nevertheless, it is noticed that each set of Nu/Nu_0 data-trend in Fig. 8 is constituted by the data points acquired from all Re tested with a fixed Ro. The respectively increasing and decreasing data trends for the channel of AR = 1 and the channels of AR = 2 and 4 are consistently observed in all the plots of Fig. 8. Acting by the buoyancy effects at a fixed Ro, the respectively improved and impaired heat transfer effects in the square and rectangular channels as have been demonstrated in Fig. 5 find the echo in Fig. 8. Magnitudes of the slopes shown in Fig. 8 vary with AR and Ro. In general, the slope for each Ro controlled data series decreases as Ro increases. Therefore the Bu effect in each test channel is weakened as Ro increases. Owing to the variety of the slopes for these Ro con-

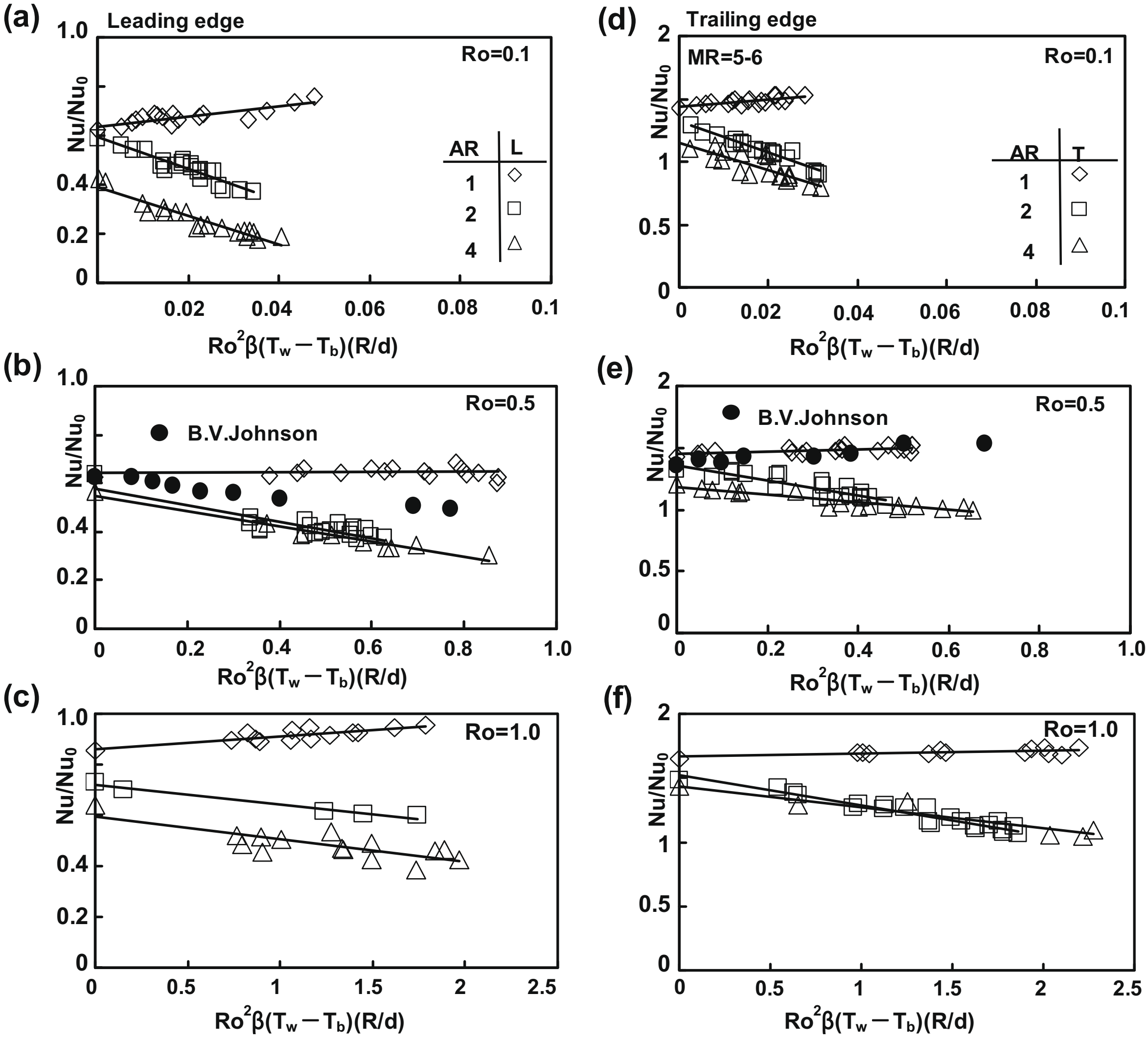

Fig. 8. Variations of Nu/Nu_0 ratios against Bu [= $\beta(T_w - T_b)Ro^2(R/d)$] in three rotating test channels of AR = 1, 2, and 4 with Ro = 0.1, 0.5, and 1 at MR 5–6 location.

trolled data trends, the *Bu* impacts are function of *Ro* and AR. The interactive *Ro*–*Bu* influence on heat transfer in each test channel is demonstrated. However, separations of *Bu* effects from the *Ro*–*Bu* complex using the direct heat transfer measurements are not practical as a finite value of $T_w - T_b$ is necessary in order to evaluate *Nu*. The so-called zero-buoyancy heat transfer levels at the limiting cases of $\beta(T_w - T_b) = 0$ but $Ro \neq 0$ are defined by extrapolating these *Ro* controlled data trends into the zero *Bu* conditions as indicated by the correlating lines added in Fig. 8. The linearly curve fitting for each *Ro* controlled data series is seen as the reasonable correlation format that leads to the generation of the asymptotic heat transfer values at the corresponding *Ro* but with zero $\beta(T_w - T_b)$. As a result, for each test channel of AR = 1, 2 or 4, the heat transfer correlations at the rib and mid-rib locations for flows in the periodically developed flow region are developed with the structure of

$$\frac{Nu_{L,T}}{Nu_0} = \phi_1\{Ro, \mathrm{AR}\} + \phi_2\{Ro, \mathrm{AR}\} \times Ro^2\beta(T_w - T_b)(R/d) \tag{4}$$

In Eq. (4), ϕ_1 and ϕ_2 are functions of *Ro* and AR. They vary with rib and mid-rib locations in the periodically developed flow region. The functional values of ϕ_1 account for the Nu/Nu_0 levels with zero-buoyancy (i.e. vanished second term) and thus signify the individual *Ro* impact on heat transfer. The various slopes for the correlating lines in Fig. 8 indexed as ϕ_2 functions reflect the manner and the degree of buoyancy impacts on heat transfer that are *Ro* dependent. The positive and negative signs for ϕ_2 values feature the improving and impeding heat transfer due to *Bu* effects respectively.

Figs. 9 and 10, respectively, depict the variations of ϕ_1 and ϕ_2 versus *Ro* at the rib and mid-rib locations in the periodically developed flow region along the leading and trailing centerlines. Data trends collected in each plot of Fig. 9 typify the sole Coriolis force effects. In each test channel, the trailing-edge ϕ_1 values vary in a form of exponential increase from unity. As AR ratio increases from 1 to 4, the ϕ_1 values at the trailing edge consistently decrease in the range of $Ro < 1$. But the ϕ_1 values for the channel of AR = 2 become higher than those of square channel as $Ro > 1$. The narrow channel of AR = 4 always shows the lowest ϕ_1 values in terms of Nu/Nu_0 ratio among the three comparative groups. It is worth noting that such diversified trends of ϕ_1 values versus AR ratio at the trailing edge are not involving with the improving *Bu* effects in the square channel and the impeding *Bu* effects in the channels of AR = 2 and 4. With the involvements of *Bu* impacts, the entire sets of Nu/Nu_0 data along the trailing edge follow the order of AR = 1, 2, and 4 as demonstrated in Fig. 6.

In the channels of AR = 1 and 2, the leading-edge Nu/Nu_0 levels quoted as ϕ_1 values in Fig. 9 are initially reduced from unity as *Ro* increases from 0 to 0.1 (not shown). In the channel of AR = 4, the ϕ_1

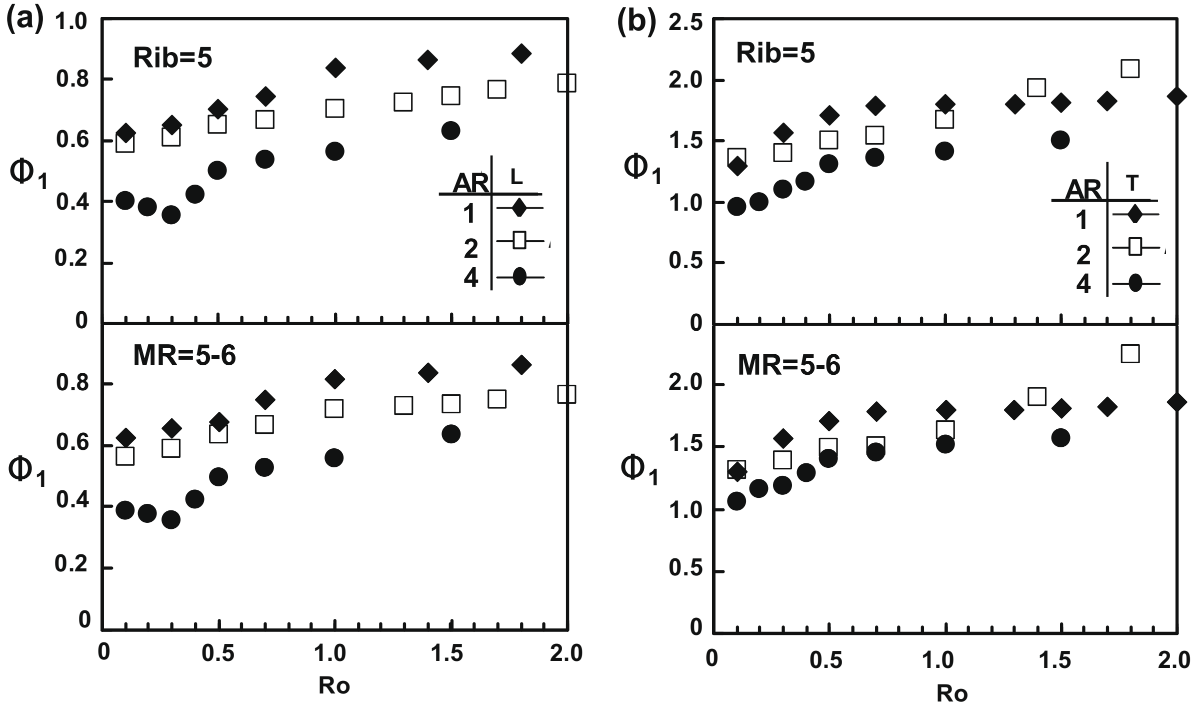

Fig. 9. Variations of ϕ_1 (Nu/Nu_0 level at zero-buoyancy condition) against *Ro* in three rotating test channels of AR = 1, 2, and 4 at Rib 5 and MR 5–6 locations.

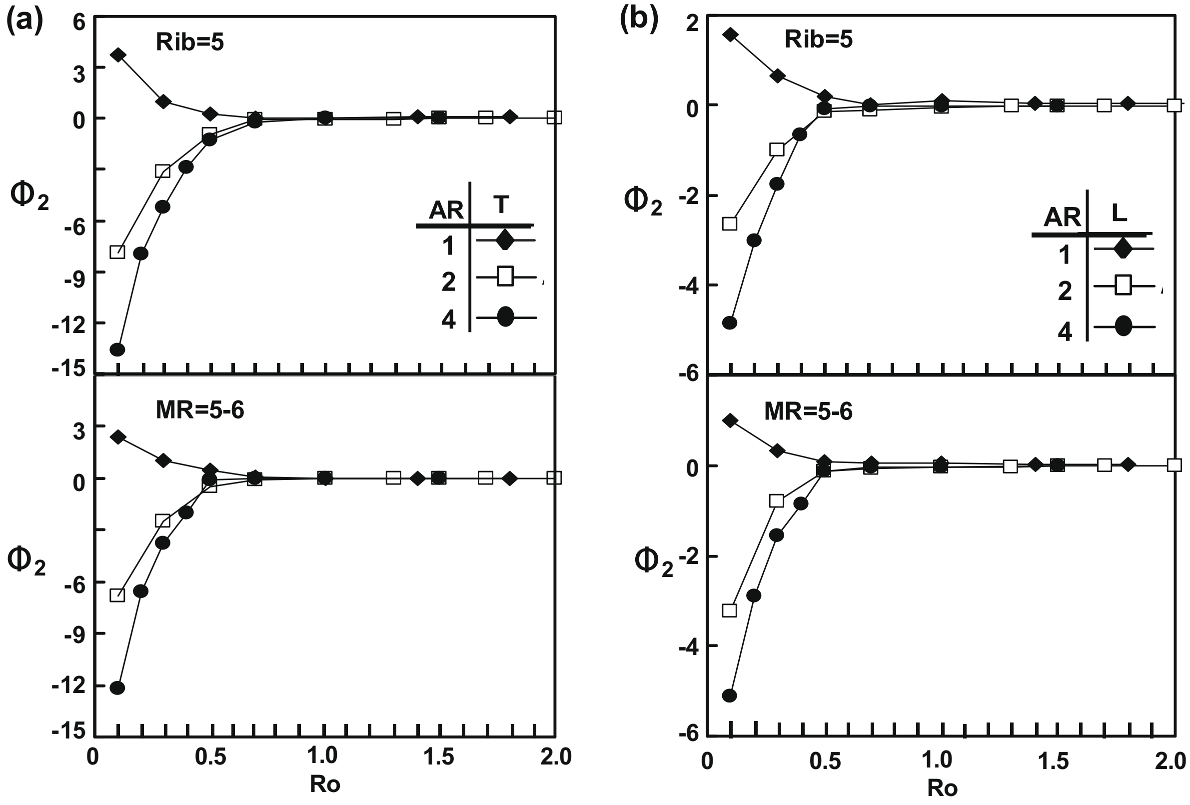

Fig. 10. Variations of ϕ_2 against *Ro* in three rotating test channels of AR = 1, 2, and 4 at Rib 5 and MR 5–6 locations.

values along the leading edge keep reducing until *Ro* is beyond 0.3. Further increases of *Ro* from 0.1 and 0.3 for the channels of AR = 1, 2 and AR = 4 respectively, the subsequent heat transfer recoveries along the leading edge are followed with the tendency to approach the zero-speed reference. Without the aids of improving *Bu* effects in the square ribbed channel, the Nu/Nu_0 levels evaluated by ϕ_1 in the derived heat transfer correlations are always less than unity on the leading wall within the parametric range of $0 \leqslant Ro \leqslant 2$. The

Table 3
Functions f_1–f_6 for $Nu_{L,T}/Nu_0$ at rib and mid-rib locations.

	Nu_L/Nu_0 (rib)	Nu_L/Nu_0 (Mid-rib)	Nu_T/Nu_0 (rib)	Nu_T/Nu_0 (Mid-rib)
f_1	$1.50 \times (\mathrm{AR}) + 5.70$	$3.26 \times (\mathrm{AR}) + 3.55$	$1.84 \times (\mathrm{AR}) + 2.60$	$2.51 \times (\mathrm{AR}) + 3.52$
f_2	$1.24 \times (\mathrm{AR}) + 5.31$	$3.02 \times (\mathrm{AR}) + 3.07$	$1.75 \times (\mathrm{AR}) + 1.72$	$2.42 \times (\mathrm{AR}) + 2.75$
f_3	$-0.27 \times (\mathrm{AR})^2 - 2.36 \times (\mathrm{AR}) + 2.20$	$-0.34 \times (\mathrm{AR})^2 - 2.45 \times (\mathrm{AR}) + 3.23$	$-0.42 \times (\mathrm{AR})^2 + 2.35 \times (\mathrm{AR}) - 5.23$	$-0.3 \times (\mathrm{AR})^2 + 2.85 \times (\mathrm{AR}) - 3.18$
f_4	$-1.08 \times (\mathrm{AR})^2 + 1.28 \times (\mathrm{AR}) - 0.18$	$0.21 \times (\mathrm{AR})^2 - 0.35 \times (\mathrm{AR}) + 0.15$	$0.40 \times (\mathrm{AR})^2 - 0.28 \times (\mathrm{AR}) - 0.04$	$2.24 \times (\mathrm{AR})^2 - 2.66 \times (\mathrm{AR}) - 0.48$
f_5	$17.86 \times (\mathrm{AR})^2 + 6.08(\mathrm{AR}) - 21.05$	$11.17 \times (\mathrm{AR})^2 + 3.05(\mathrm{AR}) - 13.82$	$32.23 \times (\mathrm{AR})^2 - 22.62 \times (\mathrm{AR}) + 17.2$	$25.63 \times (\mathrm{AR})^2 - 15.236 \times (\mathrm{AR}) + 2.36$
f_6	$-3.21 \times (\mathrm{AR})^2 + 15.23 \times (\mathrm{AR}) - 15.23$	$-4.23 \times (\mathrm{AR})^2 + 22.16 \times (\mathrm{AR}) - 25.46$	$-5.76 \times (\mathrm{AR})^2 + 29.56 \times (\mathrm{AR}) - 33.52$	$-3.97 \times (\mathrm{AR})^2 + 28.12 \times (\mathrm{AR}) - 29.96$

critical *Ro* above which the leading-edge heat transfer starts to recover is increased as AR ratio increases from 2 to 4. Beyond the critical *Ro*, the variations of leading-edge ϕ_1 values with increasing *Ro* for the three test channels also follow the general trend of exponential increase. Nevertheless, unlike the comparative results found for the trailing edge, the leading-edge ϕ_1-values signifying the sole Coriolis force effects keep decreasing as the AR ratio increases from 1 to 4.

In Fig. 8, the slope for each *Ro* controlled data trend shows the decreasing tendency as *Ro* increases from 0.1 to 2. Fig. 10 depicts the functional forms of ϕ_2 values against *Ro* for the three test channels. For each test channel, the absolute magnitudes of ϕ_2 values consistently decrease as *Ro* increases, indicating the weakened buoyancy impacts as *Ro* increases. The ϕ_2 values remain positive in the square channel of AR = 1 but turns to negative in the rectangular channels of AR = 2 and 4. These evidences reconfirm the respectively improving and impairing *Bu* effects on heat transfer in the square and rectangular channels. For $0.1 \leqslant Ro \leqslant 0.5$ Fig. 10 denotes that the increase of AR ratio from 1 to 4 reduces the ϕ_2 values from positive to negative, leading to the largest negative ϕ_2 values in the channel of AR = 4. Such ϕ_2 variations due to the modifications of flow structures in response to the increase of AR ratio are consistent along both leading and trailing edges. The detailed flow measurements to clarify such AR impacts on the *Bu* effects in the rotating ribbed channel are urged in order to unravel the responsible flow physics. Nevertheless, for $0.1 < Ro < 0.3$ the retarded heat transfer recovery along the leading edge of the narrow channel with AR = 4 as a result of the sole Coriolis force effects (Fig. 9) together with the large negative ϕ_2 values (Fig. 10) result in the worst heat transfer scenarios in terms of Nu/Nu_0 ratios, a result requiring design precautions. Such heat transfer performances in the respect of AR impacts on heat transfer for the rotating rectangular channels with skewed ribs are important for turbine designers and have never been previously reported in the open literature.

For each test channel, the combination of the parametric analysis based on Figs. 8–10 has led to a set of heat transfer correlations at rib and mid-rib locations on the leading and trailing edges in the periodically developed flow region that follows a general form of

$$\begin{aligned} Nu_{L,T}/Nu_0 = {} & f_1\{\mathrm{AR}\} - f_2\{\mathrm{AR}\} \times Exp(-f_3\{\mathrm{AR}\} \times Ro) + (f_4\{\mathrm{AR}\} \\ & - f_5\{\mathrm{AR}\} \times Exp(f_6\{\mathrm{AR}\} \times Ro) \times Bu) \\ & \text{at rib or mid} - \text{rib location} \end{aligned} \tag{5}$$

The f_1–f_6 appearing in Eq. (5) are functions of AR. Table 3 summarizes the correlated f_1, f_2, f_3, f_4, f_5 and f_6 functions within the range of $1 \leqslant \mathrm{AR} \leqslant 4$.

This set of heat transfer correlations has been derived to represent all the heat transfer measurements generated by this study. Centerline Nu/Nu_0 ratios at the rib and mid-rib locations in the periodically developed flow region of rotating rectangular channels with skewed ribs of $1 \leqslant \mathrm{AR} \leqslant 4$ can be evaluated when the controlling parameter such as *Re*, *Ro* or *Bu* varies individually or simultaneously. The comparison of all the experimental measurements with the correlative predictions as shown in Fig. 11 is performed to examine the overall success of heat transfer correlations derived. As indicated in Fig. 11, 95% the experimental data is found to agree within ±30% of the correlation proposed for the three test sections over the entire range of test conditions. The review of the entire set of heat transfer data collected form the three rotating rectangular ribbed channels in terms of Nu/Nu_0 ratios indicates that the local Nusselt number ratios (Nu/Nu_0) for the test channels of AR = 1, 2, and 4 are respectively in the ranges of 0.6–1.6 and 1.0–2.2, 0.5–1.4 and 1.1–2.7, and 0.5–1.3 and 1.0–2.1 on the leading and trailing edges to reflect the interactive *Ro*–*Bu* effects on heat transfer. In view of being able to take account of the complexities induced by the surface ribs, Coriolis force, rotating buoyancy and channel aspect ratio (AR) over such wide range of rotation num-

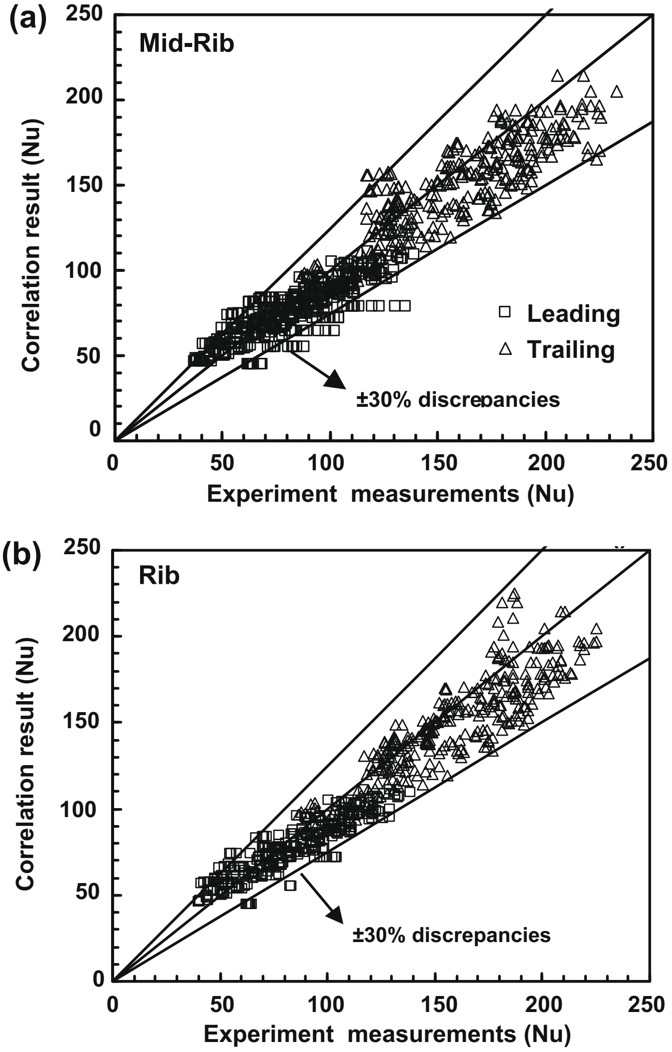

Fig. 11. Comparison of correlation results with experimental measurements along leading and trailing edges at (a) mid-rib and (b) rib locations.

bers, it is believed that the derived set of heat transfer correlations can offer the references for designing internal cooling channels in a gas turbine rotor blade.

4. Conclusions

Experimental Heat transfer results with large ranges of rotation ($Ro = 0–2.0$) and buoyancy (0.005–8.879) numbers for a rectangular ducts with 45° staggered ribs have been examined in the attempts to reveal the AR impacts on the individual Coriolis force effects and the isolated rotating buoyancy effects. The concluding remarks resulting from the present investigation are summarized as follows:

1. Due to the increased rib-height to channel-height ratio from 0.1, 0.13, to 0.16 for three stationary ribbed channels of AR = 1, 2, and 4, the Nu_0/Nu_∞ ratios fall respectively in the ranges of 2.2–2.9, 1.6–4.3, and 2.4–4.7 for $Re = 5000–15{,}000$.
2. Similar to the previous findings, as *Ro* increases the heat transfer levels along the trailing edge are consistently improved from the zero-rotation references whereas the leading-edge heat transfer levels are initially reduced from the zero-rotation references but recovered as *Ro* exceeds the critical values. The present study further shows that the values of critical *Ro* are 0.1, 0.1 and 0.3 for the test channels of AR = 1, 2, and 4, respectively.
3. Acting by the Coriolis force effects alone, the Nu/Nu_0 ratios evaluated by $\phi\phi_1$ in the derived heat transfer correlations consistently decrease in the range of $Ro < 1$ as AR ratio increases from 1 to 4 along the trailing-edge centerline. The trailing-edge ϕ_1 values for the channel of AR = 2 turn to be higher than those of square channel as $Ro > 1$. The lowest $\phi\phi_1$ values along the trailing edge constantly develop in the narrow channel of AR = 4. Along the leading-edge centerline, the ϕ_1 values are always less than unity for $0 \leqslant Ro \leqslant 2$ and keep decreasing as the AR ratio increases from 1 to 4.
4. The isolated *Bu* impacts respectively improve and impair heat transfer performances in the square and the rectangular channels of AR = 2 and 4. For $0.1 \leqslant Ro \leqslant 0.5$ the increase of AR ratio from 1 to 4 is found to considerably reduce the ϕ_2 values in the derived heat transfer correlations from positive to negative, leading to the largest negative $\phi\phi_2$ values in the channel of AR = 4. For $0.1 \leqslant Ro \leqslant 0.3$ the retarded heat transfer recovery along the leading edge of the narrow channel with AR = 4 as a result of the sole Coriolis force effects together with the large negative ϕ_2 values result in the worst heat transfer scenarios requiring turbine blade design precautions. For $0.1 \leqslant Ro \leqslant 2.0$ the Nu/Nu_0 ratios along the leading and trailing centerlines consistently decrease with increasing AR due to the combined *Ro*–*Bu* impacts. These observations were not previously reported in the open literature.
5. For *Ro* up to 2.0, a set of heat transfer correlations has been experimentally derived for the first time to evaluate the effects of AR on the centerline Nu/Nu_0 ratios at the rib-top and mid-rib locations in the periodically developed flow region of rotating rectangular ribbed channels. The Nu/Nu_0 ratios along the leading and trailing edges for the three test channels of AR = 1, 2, and 4, respectively, fall in the ranges of 0.6–1.6 and 1.0–2.2, 0.5–1.4 and 1.1–2.7, and 0.5–1.3 and 1.0–2.1 to reflect the interactive *Ro*–*Bu* effects on heat transfer.

References

[1] S.P. Harasgama, W.D. Morris, The influence of rotation on the heat transfer characteristics of circular, triangular and square-sectioned coolant passages of gas turbine rotor blades, ASME J. Turbomach. 110 (1988) 44–50.

[2] S.W. Chang, W.D. Morris, A comparative study of heat transfer between rotating circular smooth-walled and square rib-roughened ducts with cooling application for gas turbine rotor blades, JSME Int. J., Ser. B 41 (1998) 302–315.

[3] R.J. Clifford, W.D. Morris, S.P. Harasgama, An experimental study of local and mean heat transfer in a triangular sectioned duct rotating in the orthogonal mode, ASME J. Eng. Gas Turbines Power 106 (1984) 661–667.

[4] B.V. Johnson, J.H. Wagner, Wagner, G.D. Steuber, F.C. Yeh, Heat transfer in rotating serpentine passages with trip skewed to the flow, ASME J. Turbomach. 116 (1994) 113–123.

[5] L. Al-Hadhrami, J.C. Han, Effect of rotation on heat transfer in two-pass square channels with five different orientations of 450 angled rib turbulators, Int. J. Heat Mass Transfer 46 (2002) 653–669.

[6] S.W. Chang, W.D. Morris, Heat transfer in a radially rotating square duct fitted with in-line transverse ribs, Int. J. Therm. Sci. 42 (2003) 267–282.

[7] A.Q. Mohammad, H.C. Chen, J.C. Han, A numerical study of flow and heat transfer in rotating rectangular channels (AR = 4) with 45 deg rib turbulators by Reynolds stress turbulence model, ASME J. Heat Transfer 125 (2003) 19–26.

[8] C.Y. Soong, S.T. Lin, G.J. Hwang, An experimental study of convective heat transfer in radially rotating rectangular ducts, ASME J. Heat Transfer 113 (1991) 604–611.

[9] T.C. Jen, A.S. Lavine, Laminar heat transfer and fluid flow in the entrance region of a rotating duct with rectangular cross section: the effect of aspect ratio, ASME, J. Heat Transfer 114 (1992) 574–581.

[10] A. Murata, S. Mochizuki, Effect of cross-sectioned aspect ratio on turbulent heat transfer in an orthogonally rotating rectangular smooth duct, Int. J. Heat Mass Transfer 42 (1999) 3803–3814.

[11] G. Su, H.-C. Chen, J.C. Han, J.D. Heidmann, Computation of flow and heat transfer in rotating two-pass rectangular channels (AR = 1:1, 1:2, and 1:4) with smooth walls by a Reynolds stress turbulence model, Int. J. Heat Mass Transfer 47 (2004) 5665–5683.

[12] A. Murata, S. Mochizuki, Large eddy simulation with a dynamic subgrid-scale model of turbulent heat transfer in an orthogonally rotating rectangular duct with transverse rib turbulators, Int. J. Heat Mass Transfer 43 (2000) 1243–1259.

[13] A. Murata, S. Mochizuki, Effect of cross-sectioned aspect ratio on turbulent heat transfer in an orthogonally rotating rectangular duct with angled rib turbulators, Int. J. Heat Mass Transfer 46 (2003) 3119–3133.

[14] K.M. Kim, Y.Y. Kim, D.H. Lee, D.H. Rhee, H.H. Cho, Influence of duct aspect ratio on heat/mass transfer in coolant passages with rotation, Int. J. Heat Fluid Flow 28 (2007) 357–373.

[15] S. Dutta, J.C. Han, C.P. Lee, Local heat transfer in a rotating two-pass ribbed triangular duct with two model orientations, Int. J. Heat Mass Transfer 39 (1996) 707–715.

[16] W.D. Morris, K.F. Rahmat-Abadi, Convective heat transfer in rotating ribbed tubes, Int. J. Heat Mass Transfer 39 (1996) 2253–2266.

[17] S.W. Chang, T.L. Yang, W.J. Wang, Heat transfer in a rotating twin-pass trapezoidal-sectioned passage roughened by skewed ribs on two opposite walls, J. Heat Transfer Eng. 27 (2006) 63–79.

[18] T.-M. Liou, S.W. Chang, J.H. Hung, S.F. Chiou, High rotation number heat transfer of a 45-deg rib-roughened rectangular duct with two channel orientations, Int. J. Heat Mass Transfer 50 (2007) 4063–4078.

[19] S.W. Chang, T.-M. Liou, S.F. Chiou, S.F. Chang, Heat transfer in high-speed rotating trapezoidal duct with rib-roughened surfaces and air bleeds from the wall on apical side, ASME J. Heat Transfer 130 (2008). 061702-1-061702-13.

[20] JHT Editorial Board of ASME J. Heat Transfer, Journal of Heat Transfer Policy on Reporting uncertainties in experimental measurements and results, ASME J. Heat Transfer, 115 (1993) 5–6.

[21] F.W. Dittus, L.M.K. Boelter, Publications in Engineering, University of California, Berkeley, CA 2 (1930) 443.7.

[22] W.-L. Fu, L.M. Wright, J.C. Han, Buoyancy effects on heat transfer in five different aspect-ratio rectangular channels with smooth walls and 45-degree ribbed walls, GT2005-68493, ASME Turbo Expo 2005: Power for Land, Sea and Air, June 6–9, Reno-Tahoe, Nevada, USA, 2005.

[23] S.W. Chang, T.-M. Liou, W.C. Juan, Influence of channel height on heat transfer augmentation in rectangular channels with two opposite rib-roughened walls, Int. J. Heat Mass Transfer 48 (2005) 2806–2813.

[24] K.M. Iskakov, V.A. Trushin, The effect of rotation on heat transfer in the radial cooling channels of turbine blades, Teploenergetika 32 (2) (1985) 52–55.

[25] W.D. Morris, T. Aythan, Observations on the influences of rotation on heat transfer in the coolant channels of gas turbine rotor blades Proc, Inst. Mech. Eng. 193 (21) (1979) 303–311.